ACS APPLIED NANO MATERIALS

www.acsanm.org Article

Radially Grown Graphene Nanoflakes for Tough and Strong Carbon Fiber Epoxy Composites

Anastasios Karakassides, Abhijit Ganguly, John Kelly, Preetam K. Sharma, and Pagona Papakonstantinou*

Cite This: https://doi.org/10.1021/acsanm.1c01722 Read Online

ACCESS | Metrics & More | Article Recommendations | Supporting Information

ABSTRACT: A long-standing challenge in structural material design is the simultaneous attainment of high strength and toughness, a conflicting requirement rarely met in engineering materials, with important technological applications in aerospace, defense, automobile, and marine industries. Motivated from examples in biological materials, to address this challenge, we demonstrate that strong and damage-tolerant carbon-fiber-reinforced polymers (CFRPs) can be realized via the direct growth of self-assembled radially aligned graphene nanoflakes (GNFs) on carbon fibers (CFs). Here, we report a first-of-its-kind study on the dependence of strength and toughness on the surface morphology of GNFs in CFRPs. The results indicated that fracture toughness was dependent on the density and waviness of the GNFs, whereas the tensile strength was also affected by the periodicity of the coated carbon fiber layers into the laminated structures. Notably, GNFs with reduced waviness and increased number of layers exhibited enhancement in interlaminar fracture toughness for modes I and II by 93.8% and 43.3%, respectively, whereas GNFs with increased waviness led to a marginal increase or preserved tensile strength. The highly interconnected and wavy nature of GNFs facilitated effective load transfer in both in-plane and out-of-plane directions. Moreover, the out-of-plane through-volume conductivity was remarkably enhanced by 527%. The results of this work demonstrated for the first time the unique potential of GNFs, as an excellent nanoreinforcement and electrically conducting interface, for achieving simultaneously strong, tough, and conducting multifunctional CFRP composites.

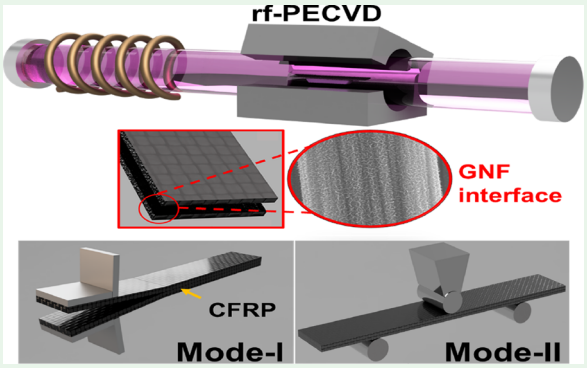

KEYWORDS: *graphene, GNFs, multifunctional composites, carbon-fiber-reinforced polymer composites, mode-I and mode-II interlaminar fracture toughness, tensile strength, electrical conductivity*

Downloaded via 86.129.167.147 on August 26, 2021 at 14:14:01 (UTC).
See https://pubs.acs.org/sharingguidelines for options on how to legitimately share published articles.

1. INTRODUCTION

Carbon fibers (CFs) have played a central role in the production of lightweight high-performance composites for a wide variety of structural applications in several sectors, including aerospace,[1] defense,[2] transportation,[3] and construction.[4] Carbon-fiber-reinforced polymer (CFRP) composites have been used in these applications due to their superior properties such as a high in-plane strength and high stiffness-to-weight ratio, dominated by fibers' properties. Nonetheless, the out-of-plane properties of the composites are controlled by the brittle nature of the epoxy resin and the weakly adhered fiber−matrix interface. As a result, under harsh operating environments, CFRPs are prone to interlaminar fracture (delamination), which is a limiting factor in the toughness and durability of the composites, severely reducing their service lifetime. Interlaminar fracture toughness tests (modes I and II)[5,6] offer approaches to assess the energy required for crack initiation and propagation by measuring delamination lengths in specimens under opening (mode-I) and sliding (mode-II) loading conditions.

This need for strong and tough materials is long-sought in structural applications. However, the design of strong and tough materials is often a trade-off as these two properties generally contradict each other.[7] This is because strength represents a material's resistance to deformation and is usually high for materials that are brittle (less tough). On the other hand, toughness requires the facilitation of stress-induced deformation (absorption of mechanical energy) and is high for lower strength materials, i.e., materials that can deform more easily. It still remains a challenge to realize high-toughness CFRPs without sacrificing strength. To tackle this challenge, insight can be gained from natural materials such as nacres, where high strength and toughness are conferred through hierarchical architectures assembled at different length scales (nanoscale to macroscale).[8] The hierarchy in nacres is developed through (i) assembly of nanoscale asperities (10−50 nm in diameter) on the

Received: June 29, 2021
Accepted: August 13, 2021

 © XXXX American Chemical Society

surface of aragonite ($CaCO_3$) brittle platelets (5−10 μm wide, ∼0.5 μm thick) and (ii) a "brick-and-mortar" layered microstructure constructed by alternate stacking of nanostructured $CaCO_3$ platelets (brick) and biopolymers (mortar). This nano/microstructure incorporates toughening mechanisms to maximize energy dissipation and relieve local stresses. The biopolymer "mortar" allows limited sliding between the platelets, which is achieved by roughening their surfaces with nanoasperities, to provide frictional stops (interlocking during the sliding). If the sliding was excessive (i.e., not limited), the material would lose its strength. Additional mechanisms such as crack deflection giving torturous crack paths, bridging, and pull-out of the mineral platelets provide additional source of toughening on much larger length scales (micrometer scale). Overall, the outstanding mechanical behavior of nacre is a result of competing mechanisms that maximize energy dissipation and relief of local stresses through the synergistic roles of the hierarchical architectures and interfaces.

Over the years, many different methods have been sought to improve the poor through-thickness properties of laminated composites and resistance to delamination, such as 3D stitching,[9−11] Z-pinning,[12] 3D weaving,[13−15] and braiding.[16] Although all these approaches present significant potential for interlaminar reinforcement, they cause fiber damage and movement of the in-plane microfibers, leading to a large degradation in composite's in-plane properties.[17] As a result, alternative routes for interlaminar reinforcement have been sought to overcome these hurdles.

Another strategy for strengthening the interlaminar region of composites that is currently gaining interest is the introduction of thin toughening layers between the carbon fabrics or plies, known as interleaving. The interleaf materials are made of micro- or nanoscale toughening thermoplastic particles or veils (e.g., polyamide, polyethersulfone, polyphenylene sulfide, aramid).[18−22] In particular, nanofiber veils, due to their highly porous structure, do not impede the resin flow during curing. Their very high specific surface areas promote good bonding with the matrix resin, whereas their lightweight and thin nature does not significantly affect the overall laminate weight and thickness. Mode-I and mode-II interlaminar toughness improves significantly, mainly due to fiber bridging, which extrinsically resists crack opening. It is generally accepted that interleaves create a phase-separated blend with the epoxy matrix and generate energy dissipation mechanisms, which can enhance the interlaminar toughness of CFRPs without decreasing the in-plane properties, with minimum weight/thickness penalty. However, there is a large variation in the reported values of enhancement for modes I and II,[18−25] as the toughening performance can be affected by many factors, including the areal density of thermoplastic interleaves (affects porosity), type of material (melted or non-melted), and architecture of CF fabrics.

Blending graphene nanoplatelets and carbon nanotubes (CNTs) into the polymer matrix has been identified in recent years as a popular way to toughen the interlaminar region due to the high specific strength and modulus of the nanomaterials.[26−32] Even though, this process is compatible with the existing composite manufacturing processes, the resulting composites generally suffer from low nanomaterial loadings (typically <1% volume fractions) due to increased resin viscosity and associated agglomeration at high nanofiller content.[33]

Several works, including CNT grafting onto CFs or prepregs by spraying,[34] have overcome these limitations and demonstrated improved interlaminar mechanical properties of CFRPs when subjected to loading modes I and II. In addition, CNT veils[35] can increase mode-I interlaminar fracture toughness energy (G_{IC}) by impeding crack propagation and inducing fiber bridging. Transfer of aligned CNT forests directly on prepregs maintained the in-plane strength of the composites while yielding 100% and 200% higher fracture energy values for the respective modes by nanostitching the plies together.[36]

Mimicking the nacre's nanostructure, vertically aligned graphene nanoflakes (GNFs) directly grown on CFs[37−40] have captured attention as a nanoscale reinforcement for high-performing aerospace structures. GNFs exhibit a three-dimensional (3D) interconnected open porous structure, with a high density of edge planes consisting of a few graphene layers.[41,42] Importantly GNFs can be grown directly on CFs via the plasma-enhanced chemical vapour deposition (PECVD) method without the need for a catalyst, representing a significant cost benefit for large-scale production over other carbon reinforcements such as aligned CNTs. Measurements on single fiber experiments have demonstrated that the interfacial shear strength between the CF and epoxy could be improved significantly in the range of 101.5−222.8%,[37−40] with modest degradation of the tensile strength of the CF. In particular, in our earlier study,[39] we discovered that when GNF growth is conducted in a high-temperature microwave PECVD plasma, a remarkable increase of 28% in tensile strength was observed, accompanied by a rapid growth rate. Similar to nanotubes, the high electrical and thermal conductivity of GNFs provides multifunctional capabilities to the resultant composites, such as monitoring of structural damage, electromagnetic interference shielding, prevention of electrostatic discharges, lightning strike protection, and deicing, as well as potential for structural energy storage.[39] So far, previous research has demonstrated the benefits of GNFs on single fiber experiments. Results on laminate structures to investigate the interlaminar fracture toughness, tensile strength, and underlying mechanisms still remain unknown. Importantly, the effect of waviness formed in GNFs or density of flakes in CFRPs is largely unexplored.

In this work, for the first time, to explore interlaminar behavior and obtain a deeper understanding of the multiscale GNF reinforcement mechanisms, mode-I and -II fracture behavior of CFRP incorporating GNFs with different degrees of GNF waviness and density was investigated by conducting double cantilever beam (DCB) and end-notched flexure (ENF) tests. In addition, in-plane strength and stiffness enhancement were assessed via standard tensile measurements on laminates. SEM was used to study the damage following the mechanical tests. Finally, the out-of-plane electrical conductivity was also assessed. Unique insights gained from this work enabled a better understanding of reinforcement mechanisms at work and helped us to guide the design of future nanoreinforced CFRPs.

2. MATERIALS AND METHODS

2.1. Materials. In this work, the CF plain fabrics (Pyrofil TR30S 3k, Mitsubishi Chemical Corporation, Tokyo, Japan) were supplied by Easy Composites Ltd. (Longton, Stoke-on-Trent, Staffordshire, U.K.), possessing an areal weight of 210 g m^{-2}. Conductive silver paint (PELCO Conductive Silver Paint) was utilized for electrical conductivity measurements, purchased from Agar Scientific Ltd. (Stansted, Essex, U.K.). The epoxy resin used for the manufacturing of the laminates was an IN2 epoxy infusion resin with an AT30 slow hardener (3-aminomethyl-3,5,5-trimethylcyclohexylamine + trimethylhexane-1,6-diamine + benzyl alcohol) from Easy Composites Ltd. All gases used in this study (Ar and CH_4) were purchased from BOC Ltd. (Guildford, Surrey, England, U.K.).

https://doi.org/10.1021/acsanm.1c01722
ACS Appl. Nano Mater. XXXX, XXX, XXX−XXX

2.2. Direct Growth of GNFs on CFs by Radio Frequency Plasma-Enhanced CVD. The growth of GNFs was performed with a 13.56 MHz PT-O1200-4C rf-PECVD system, supplied by Zhengzhou Protech Technology Co. Ltd. (Zhengzhou City, China), with argon (Ar) and methane (CH_4) as the primary feed gases. The CF fabrics were placed on a 25 cm long custom-made quartz boat holder, which was positioned carefully in the middle of the furnace tube with the help of a metallic guide. When the background pressure in the chamber reached ~7.5×10^{-3} Torr, Ar (30 sccm) was introduced to achieve the desired pressures of 1.8×10^{-2} and 3×10^{-2} Torr. The temperature in the tube furnace was increased to 800 °C at a heating rate of 20 °C min^{-1}. When the temperature of 800 °C was reached, 10 sccm of CH_4 was introduced into the chamber and GNF growth was initiated by striking of the plasma at a power of 500 W for durations of 30 and 60 min. Following the GNF growth, a constant Ar flow (30 sccm) was used to cool the deposited CFs. Three laminates, prepared with GNFs under different deposition conditions, were considered for the investigation of interlaminar fracture toughness and tensile strength. In the following discussion, bCF denotes the as-purchased CF fabric, which acts as the reference specimen; G-1LP denotes CF/GNF hybrid fabric synthesized at a temperature of 800 °C, a radio frequency power of 500 W, a total pressure of 1.8×10^{-2} Torr with 10 sccm of CH_4, and a deposition time of 1 h (1 h at 1.8×10^{-2} Torr). Likewise, G-0.5LP was fabricated at 800 °C, 500 W, and 1.8×10^{-2} Torr with 10 sccm of CH_4 for 0.5 h (0.5 h at 1.8×10^{-2} Torr), and G-0.5HP was fabricated at 800 °C, 500 W, and 3×10^{-2} Torr with 20 sccm of CH_4 for 0.5 h (0.5 h at 3×10^{-2} Torr) (Table S1). To evaluate the impact of deposition time on the structural, mechanical, and electrical properties, G-1LP and G-0.5LP were deposited under identical conditions with only change in the coating GNF growth (G-1LP and G-0.5LP). For G-0.5LP and G-0.5HP, the deposition time, power, and temperature were kept the same; however, the total pressure and CH_4 flow were different.

2.3. Characterization of Materials. The surface morphology of grown GNFs onto CFs and the delaminated samples after the fracture toughness tests were examined through a field emission scanning electron microscope (FESEM, HITACHI SU5000, Tokyo, Japan) working at accelerating voltages of 10 kV (GNF/CF hybrids) and 1 kV (fractured samples). Transmission electron microscopy measurements (TEMs) were performed on a Jeol JEM-2100F field emission system at 200 kV. For TEM measurements, the graphene flakes were scratched off the carbon fibers and suspended in methanol before drop-casting on a lacey carbon grid. X-ray diffraction (XRD) measurements were performed on a Panalytical Empyrean Series 3 system in the 10−35° range at a grazing incidence of 2°. Raman scattering was utilized to investigate the electronic structure of GNFs as well as any variations on the surface of CF/GNFs fabrics, using a Renishaw Invia Qontor system (Renishaw plc, Gloucestershire, U.K.), operating at the 532 nm excitation wavelength (RL532C laser source).

2.4. Vacuum-Assisted Resin Infusion Procedure. The CFRP specimens were manufactured utilizing a vacuum-assisted resin infusion (VARI) process at room temperature. VARI is a straightforward and relatively low-cost process in comparison with other lamination procedures (wet lay-up, prepreg, hot press lamination, filament winding, etc.). Some of the advantages of this method are (i) minimum air voids in the composite structures due to the infusion procedure and (ii) large-scale production of composite components. The epoxy resin (IN2) and hardener (AT30) were manually mixed at a weight ratio of 100:30 as recommended by the resin supplier. All fabricated laminates consisted of a total 12 plies, laid up in a stacking sequence of 0°/90° ($[0/90]_{12}$). All samples were fabricated and cured initially at room temperature for a period of 24 h. After the initial curing, the CFRPs were post-cured for 6 h at 60 °C, in accordance with the manufacturer's guidelines. The 3 mm thick produced laminates were cut into appropriate sizes for the three different tests under investigation ($L_{\text{mode-I}} \times W_{\text{mode-I}} = 12.5$ cm × 2 cm; $L_{\text{mode-II}} \times W_{\text{mode-II}} = 19$ cm × 2 cm; and $L_{\text{tensile}} \times W_{\text{tensile}} = 21$ cm × 2 cm). For mode-I and mode-II interlaminar fracture toughness tests, two GNF-coated CF fabrics were placed on the intermediate area of each laminate, facing each other, resulting in a new reinforced interface. For tensile strength measurements, two different lay-up configurations were selected. The first configuration contained, in total, four CF/GNF fabrics, with two of these fabrics placed in the middle plane of the laminate, facing each other, and creating a GNF−GNF interface in the interlaminar region, whereas the remaining two CF/GNF fabrics were placed at the outer sides of the laminate facing the environment, as depicted in Figure S2a. The second configuration depicted in Figure S2b contained, in total, eight CF/GNF fabrics, with six of these fabrics facing each other, creating three GNF−GNF reinforcing interfaces, while the remaining two fabrics were placed at the outer sides of the laminate facing the environment.

2.5. Mode-I Interlaminar Fracture Toughness Measurements. The merit of introducing GNFs onto the CFs, for reinforcing the composite, was assessed using three forms of mechanical testing. Initially, mode-I interlaminar fracture toughness was obtained through the DCB technique according to the ASTM D5528-13[5] standard. The geometry and dimensions of a DCB specimen are illustrated in Figure S7.

A 70 mm long and 0.025 mm thick Teflon nonadhesive film was introduced prior to the lamination process in the midplane region of each composite to create an initiation site for the delamination with a precrack length (a_0) of 50 mm, as illustrated in Figure S8. Two piano hinges, 20 mm long and 20 mm wide, were attached on the two sides of each laminate using high-strength epoxy glue (Araldite Epoxy Adhesive) that was cured at 25 °C for 24 h. Five set of specimens were fabricated and loaded on a Universal Instron tensile tester (model 5500R) operating under a constant displacement rate of 1 mm min^{-1} and a maximum load capacity of 5 kN. With the help of a travelling USB camera, the applied force (P), crosshead displacement (δ), and the crack length (a) were recorded. Mode-I analysis included two different interlaminar fracture toughness values: one deduced from the initiation process of the crack, which presents the initiation fracture toughness ($G_{\text{IC,INIT}}$), and one originating from the propagation of the crack after the initiated crack growth, which presents the propagation fracture toughness ($G_{\text{IC,PROP}}$). Initially, each specimen was loaded until the initial crack tip was delaminated by 3−5 mm (Figure S8). Then, the sample was reloaded with the same crosshead speed, until the final delamination growth length (~50 mm) was reached. Subsequently, utilizing a Java-based image processing software (ImageJ), the crack growth of each specimen was calculated. A small metallic ruler (15 cm total length) was attached onto one Instron clamp to provide a scale for the image processing data analysis, as presented in Figure S8.

The edges of the samples were covered with white paint to enable better detection of the crack growth. The load P (N), vertical crack opening displacement δ (mm) of the piano hinges, and delamination length a (mm) were recorded and utilized to calculate the mode-I interlaminar fracture toughness (G_{IC}) values according to the modified beam theory (MBT) approach.[5] The traditional beam theory (BT) method overestimates the mode-I fracture toughness value, since it does not take into account possible rotation at the cck front during the DCB test. This is corrected in MTB by including a crack correction length, Δ (i.e., $a + |\Delta|$ instead of just a). The MBT data reduction method yields a more conservative value of G_{IC}, which is described by the following expression:

$$G_{\text{IC}} = \frac{3P\delta}{2b(a + |\Delta|)}F \tag{1}$$

where b is the specimen width, P is the load, δ is the vertical crack opening displacement, and $a + |\Delta|$ is the corrected delamination length. $|\Delta|$ is determined as the intersection point on the x axis of the linear regression data when plotting the cube root of compliance C of the arms of the specimen ($C^{1/3} = (\delta/P)^{1/3}$) against the delamination length (a). F is the correction factor that accounts for large displacement and shortening of the moment arm of the test specimens.

2.6. Mode-II Interlaminar Fracture Toughness Measurements. Mode-II interlaminar fracture toughness, G_{IIC}, under pure shear loading conditions of the produced laminates was investigated using the ENF test in compliance with the ASTM D7905/D7905M-14[6] standard (Figure S9).

A Teflon nonadhesive film of 75 mm length (a_i) and a thickness of 0.025 mm was inserted at the specimen midplane to initiate

https://doi.org/10.1021/acsanm.1c01722
ACS Appl. Nano Mater. XXXX, XXX, XXX−XXX

Scheme 1. Schematic Illustration of the CFRP's Fabrication Process[a]

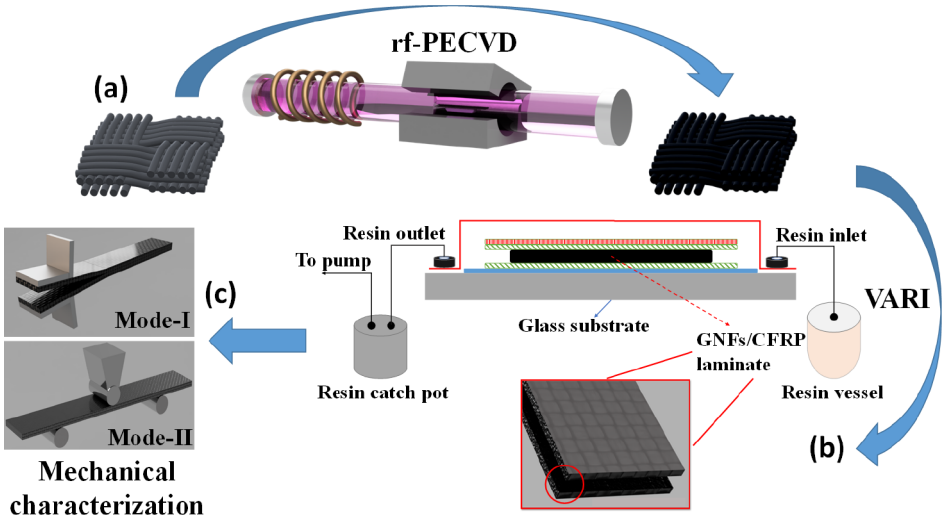

[a](a) Growth process of the GNFs on the CF fabrics via radio frequency PECVD (rf-PECVD), (b) CFRP fabrication through vacuum resin infusion, and (c) mechanical characterization of the produced laminates.

delamination. A Universal Instron loading machine (same used for mode-I tests) was used to apply a force at a three-point bending configuration, using a 5 kN load cell, at a constant displacement rate of 0.5 mm min^{-1}. During the test, the applied force (P) and crosshead displacement (δ) were recorded. Mode-II measurements included two different G_{IIC} tests. In the first test, called non-precracked (NPC) test, the crack was generated from a preimplanted insert (nonadhesive film), whereas in the second test, called precracked (PC), the delamination was advanced on the same specimen that was subjected to the NPC test. On both tests, compliance calibrations (CCs) had to be determined according to the standard.[6] The first CC test was performed with a crack length, a, equal to 20 mm, following the procedure defined in the standard. The specimen was then repositioned to a = 40 mm and finally repositioned again in the fixture so that a_0 = 30 mm, which was the last CC test, called fracture test. Hence, in total, three CC tests were performed, as depicted in Figure S9 (three green-lined CC marks are indicated, beneath the left roller of the system). In the third CC test (a_0 = 30 mm), the sample was loaded until development of delamination, which was detected on the specimen (3−5 mm crack length) either visually or by a drop in the load on P vs δ graph. After the NPC test, the new crack tip was marked with a pen to start the PC test (Figure S10). The same procedure was used in order to determine the CCs for the PC test as well.

Subsequently, the three NPC compliances were plotted versus the cubed value of the crack length. The three compliances were determined from the two CC tests (at a = 20 and 40 mm) and from the fracture test (a_0 = 30 mm). At each crack length, the compliance was assessed through a linear regression analysis to obtain the slope of δ versus P data. For the two CC tests, this regression analysis included all data for which P was larger than or equivalent to 90 N, including the peak force used during the test. For the fracture test, the regression analysis (curve-fit) included all data for which the force was larger than or equivalent to 90 N and less than or equivalent to 50% of the maximum force from the fracture test. The CC coefficients, A and m, were determined using a linear regression analysis of the C vs a^3 data presented below:

$$C = A + ma^3 \tag{2}$$

where A is the intercept and m is the slope obtained from the regression analysis. The PC CC coefficients were evaluated in the same way as the NPC CC ones. The calculation of the mode-II interlaminar fracture toughness for both NPC and PC tests was performed using the following equation:

$$G_{IIC} = \frac{3mP_{max}{}^2 a_0{}^2}{2B} \tag{3}$$

where m is the CC coefficient, P_{max} is the maximum force from the fracture test, a_0 is the crack length used in the fracture test (30 mm), and B is the specimen width.

2.7. Tensile Strength Measurements. To assess the impact of GNFs on the tensile strength of CFRPs, five specimens of each experimental set were subjected to tensile testing according to ASTM D3039/D3039M-17.[43] For the tensile strength measurements of the CFRP specimen, the equations used for the calculation of the experiment's key parameters (tensile strength and strain) were calculated as follows:

$$T = \frac{F}{A} \tag{4}$$

$$\varepsilon = \frac{\Delta l}{l_0} \tag{5}$$

where T (Pa) is the tensile strength, F (N) is the force to failure, A (m^2) is the fiber's cross-sectional area at the fracture plane (normal to fiber axis), Δl (mm) is the elongation of the gauge length, and l_0 (mm) is the gauge length. The system used for the tests was again the Instron 5500R, with the only difference that the load cell of the machine was selected at 100 kN.

For better accuracy of the displacement monitoring, an external extensometer (model 3542, Epsilon technology Corp., U.S.) was used (Figure S12), avoiding in that way any possible errors that could occur during the measurement originating from the sliding effects on the gripping area of the samples. For the better gripping of the specimen, glass-fiber-reinforced polymer (GFRP) end tabs were used, avoiding with this way any damage that could occur at that area by the compressive forces that were developed by the grips of the machine. The fabrication of the end tabs was done in the following way: 12 layers of glass fiber plain fabric (of 290 g m^{-2} areal weight purchased from Easy Composites Ltd., U.K.) were utilized, and the final thickness of the tabs was about 3 mm. The tabs were mounted onto the sides of the CFRP specimen using an epoxy adhesive glue.

2.8. Electrical Conductivity Measurements. Electrical conductivity measurements were performed on the CFRP utilizing a two-probe Keithley 2611B system source meter. The electrical conductivity of the CFRP was calculated using the subsequent equation:

$$\sigma = G\frac{L}{A} \tag{6}$$

https://doi.org/10.1021/acsanm.1c01722
ACS Appl. Nano Mater. XXXX, XXX, XXX−XXX

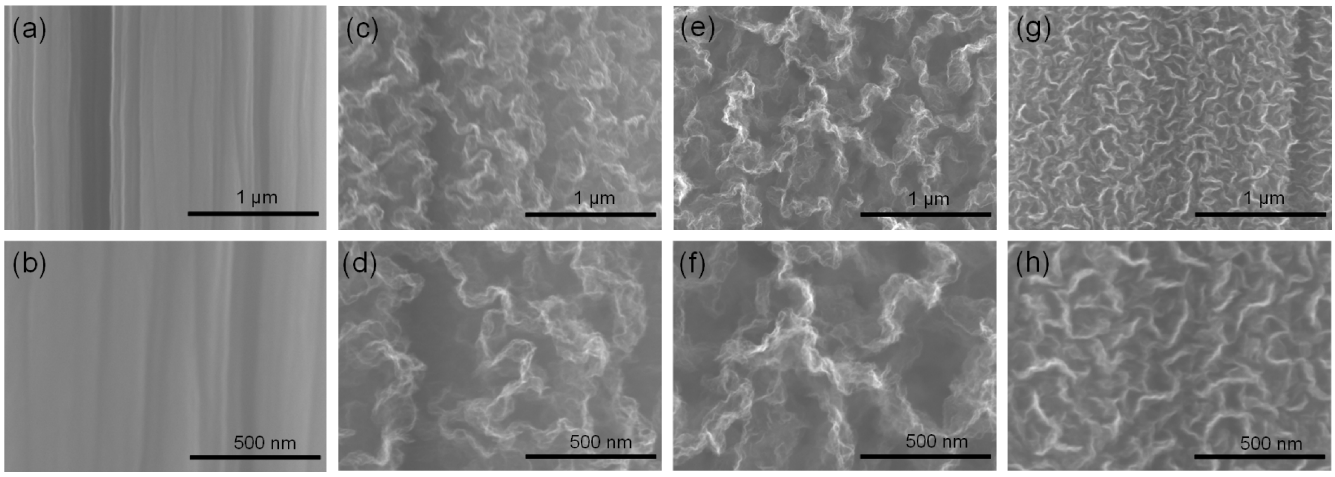

Figure 1. SEM micrographs of the grown GNFs. (a and b) bCF (reference sample), (c and d) G-0.5LP sample (0.5 h at 1.8×10^{-2} Torr), (e and f) G-1LP sample (1 h at 1.8×10^{-2} Torr), and (g and h) G-0.5HP (0.5 h at 3×10^{-2} Torr).

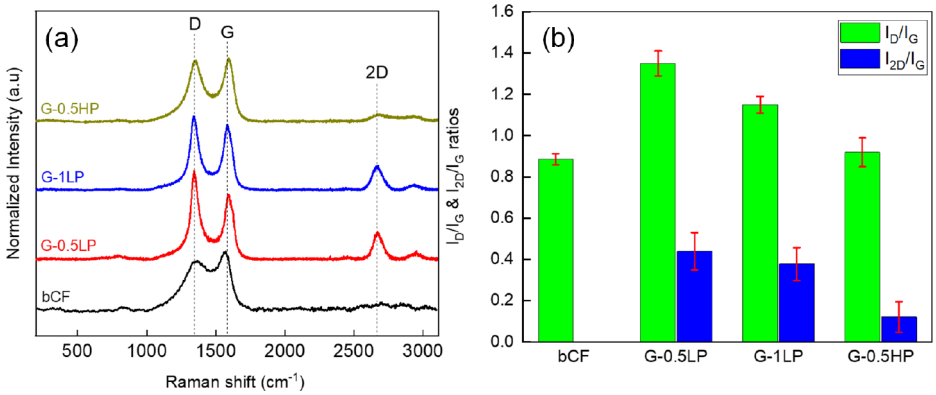

Figure 2. Raman characterization of the produced GNFs. (a) Raman spectra of all samples and (b) I_D/I_G intensity ratios of all samples. bCF (reference sample), G-0.5LP sample (0.5 h at 1.8×10^{-2} Torr), G-1LP sample (1 h at 1.8×10^{-2} Torr), and G-0.5HP sample (0.5 h at 3×10^{-2} Torr).

where σ is the electrical conductivity (S cm^{-1}), L is the length between the two contacts, G is the conductance (S), and A is the cross-sectional area (cm^2).

Both in-plane and out-of-plane through-volume electrical conductivities on the fabricated laminates were determined. The different probe contacts for each configuration can be seen in Figure S13. It should be noted that for better contact between the crocodile clips of the source meter and the CFRP specimens, the CFRP's surface was polished slightly with the help of a file. After polishing, conductive paste was placed, and above it, copper tape strips were placed, creating a consistent and more conductive connection among the crocodile clips and the laminates.

3. RESULTS AND DISCUSSION

3.1. SEM and Raman Characterization. Control on the detailed characteristics [including density, length, height, and width (number of layers)] of GNFs is of crucial importance for enhancing the mechanical properties of the composite. SEM micrographs were used to assess the morphology of the grown GNFs onto CFs and hence gain insight into the growth condition−morphology−property relationship triangle. As mentioned earlier, G-1LP and G-0.5LP were deposited under identical deposition conditions except for the GNF growth time (G-1LP, 1 h; G-0.5LP, 0.5 h). On the other hand, G-0.5LP and G-0.5HP were grown under the same deposition time (0.5 h), power (500 W), and temperature (800 °C); however, the total pressure (G-0.5LP, 1.8×10^{-2} Torr; G-0.5HP, 3×10^{-2} Torr) and CH_4 flow rate (G-0.5LP, 10 sccm; G-0.5HP, 20 sccm) were different.

It should be noted that GNF growth was confined only on the top surface of the fabric, since the opposite side was shielded from the plasma by the quartz boat, which served as a substrate holder for positioning the fabric inside the tube. In addition, no GNFs were found on the interior fiber rows since these were protected by the outer fibers, which acted as a shield, preventing reactive fluxes reaching the inner fibers.

Figure 1c−h shows the SEM images of GNFs grown on CFs under the three selected deposition conditions. All three samples exhibit a self-assembled network of vertically aligned graphene nanosheets with a labyrinth-like morphology. The bare CF (Figure 1a,b) has an average diameter of ∼7 μm, with evident surface grooves originating from the CF manufacturing process. G-1LP and G-0.5LP, which were synthesized under identical conditions, except for the growth time, possessed a similar corrugated morphology but different coating thicknesses (1.78 and 1.02 μm, respectively), consistent with their growth times (larger thickness for longer deposition). In contrast, G-0.5HP, which was fabricated under different pressures (higher total pressure and higher CH_4 flow rate), exhibited a higher density of nanoflakes with a less wavy appearance and reduced coating thickness (∼0.72 μm). The lower thickness (∼0.72 μm) at higher pressures is evident from the presence of visible grooves from the underneath fiber and is associated with a reduced

https://doi.org/10.1021/acsanm.1c01722
ACS Appl. Nano Mater. XXXX, XXX, XXX−XXX

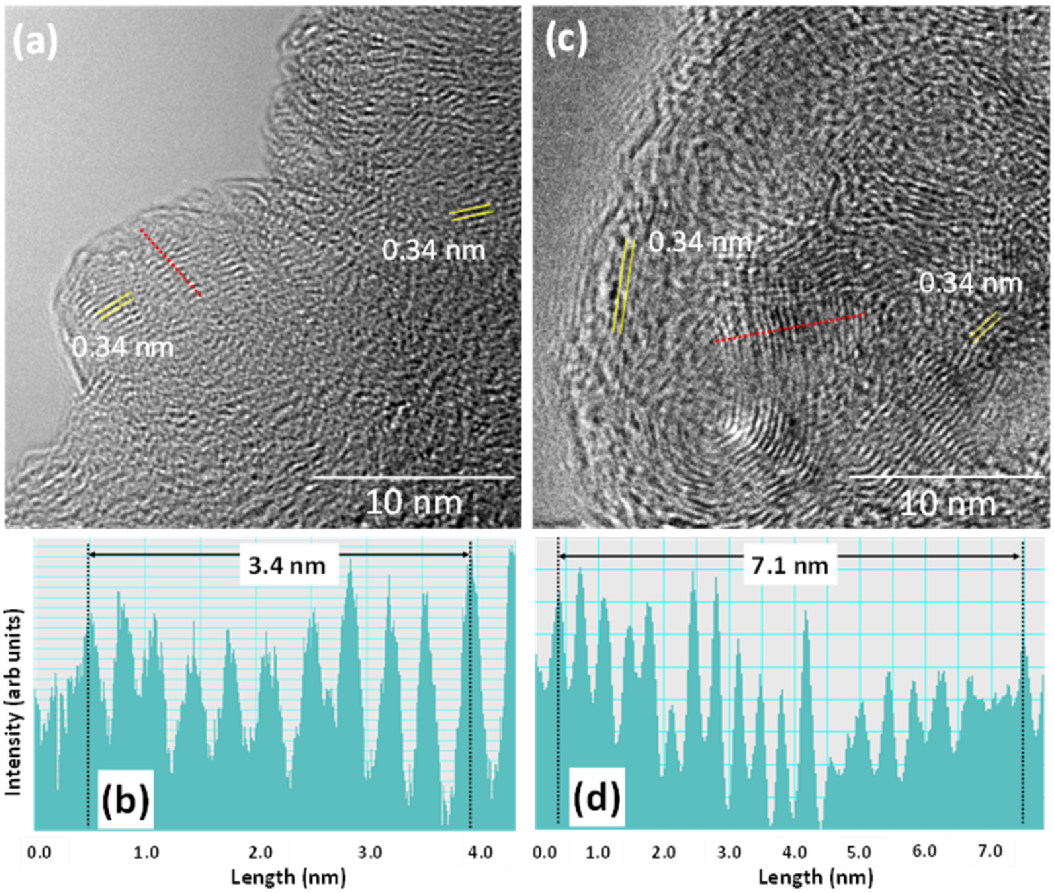

Figure 3. TEM analysis of G-1LP and G-0.5HP samples. (a) G-1LP sample and (c) G-0.5HP sample. (b) G-1LP intensity profile of planes depicted by the red line in (a) and (d) G-0.5HP intensity profile of planes depicted by the red line in (c).

dissociation rate of the precursor.[44] It should be noted that during the deposition of the G-0.5HP sample, the plasma was not filling the tube completely, in contrast to deposition of G-1LP and G-0.5LP where the plasma was extending through the whole tube length. The dense network of more straight (less corrugated) nanosheets for G-0.5HP compared to that for G-1LP and G-0.5LP is obvious from the 3D illustrations of the SEM micrographs, which were constructed with the help of an open-source software for scanning probe microscopy data analysis (Figure S1). Out-of-plane deformations in graphene sheets in the form of wrinkles or crumples were induced by lattice and/or thermal mismatches between the fiber and the graphitic layers, as well as topological defects.[45] In contrast, in G-0.5HP, the corrugation of graphene flakes is less prominent; however, it possesses a higher density of smaller, branched flakes with reduced voids.

Raman spectroscopy was performed on the coated CF fabrics to assess the presence of defects and number of layers (i.e., graphitic quality of the nanoflakes).[46] All acquired spectra (Figure 2a) consisted of prominent vibrational modes, observable near 1345 cm^{-1} (D band), 1580 cm^{-1} (G band), and 2690 cm^{-1} (2D band).[47−49] The D band results from the existence of various types of defects at grain boundaries between graphene crystals[50] or at wrinkles, in-plane substitutional heteroatoms, vacancies, and edge plane sites. It originates near the K point of the Brillouin zone, possessing transverse optical (TO) vibrations. The G band is representative of sp^2 bonding, it originates from first-order Raman scattering, and it is due to strain in the C−C bond of graphitic networks. The 2D band is a result of a double-resonance (two phonons near the K point) Raman process.

A common tool for the crystalline quality evaluation of graphitic structures is the intensity ratio of the D band to the G band (I_D/I_G), which is ideally zero for highly ordered pyrolytic graphite.[46] The lowest I_D/I_G ratio of 0.91 observed for G-0.5HP (Figure 2b) grown at higher pressures indicates the lowest number of defects among the three samples, whereas the higher values observed at lower pressures for samples G-1LP and G-0.5LP (1.5 and 1.35, respectively) are consistent with the prominent corrugated texture of the graphene flakes. An I_{2D}/I_G ratio greater than or equal to 2 is indicative of single-layer graphene, whereas lower values are associated with multilayer graphene.[39,51] Hence, the low I_{2D}/I_G ratio values observed for all samples (<1) reveal a large number of graphene layers in the nanoflakes. The lowest I_{2D}/I_G ratio of the G-0.5HP (0.121) sample correlates well with the TEM analysis (Section 3.2), which revealed a larger number (∼20) of graphene layers, when compared to the other samples. In addition, further confirmation for the larger number of layers in G-0.5HP is provided by the full width at half-maximum (FWHM) values of the deconvoluted Raman bands (Figure S3 and Table S2), where it can be seen that the FWHM for the 2D band was increased for the G-0.5HP sample (107.8 vs 82.8 for G-0.5LP and 92.8 for G-1LP). The lower position of the 2D band for the high-pressure sample G-0.5HP (2665 cm^{-1}) compared to the low-pressure ones (G-0.5LP, ∼2675 cm^{-1}; G-1LP, 2669 cm^{-1}) indicates that graphene layers are in compression.[52] This compressive stress is relieved by extensive wrinkling as evidenced by the SEM images

https://doi.org/10.1021/acsanm.1c01722
ACS Appl. Nano Mater. XXXX, XXX, XXX−XXX

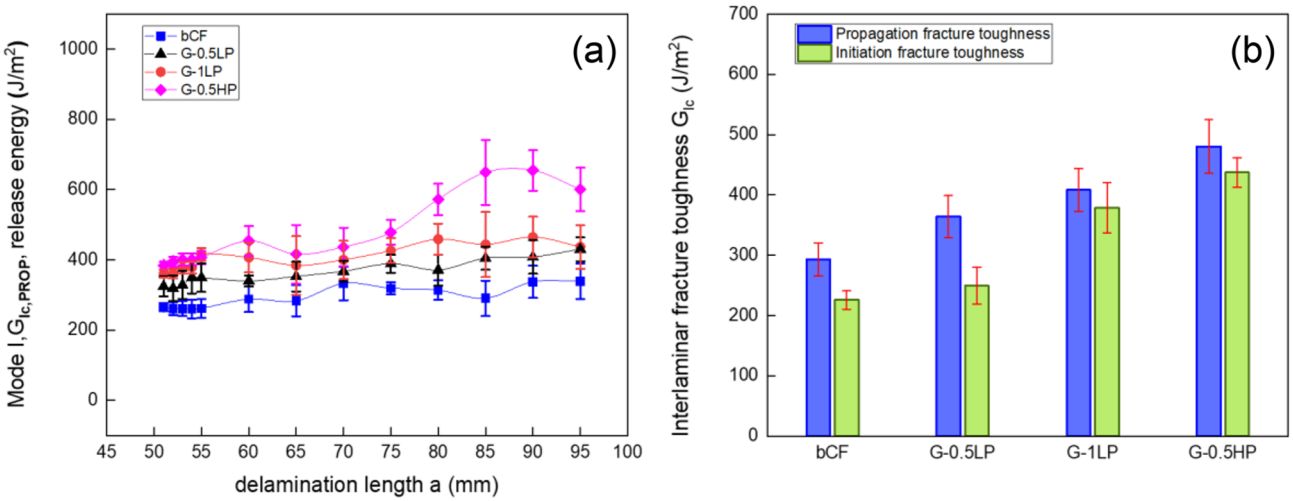

Figure 4. Mode-I interlaminar fracture toughness analysis. (a) *R* curves for reference (bCF) and all fabricated samples (G-0.5LP, G-1LP, and G-0.5HP; the lines connecting the data points were constructed for their better visual observation) and (b) $G_{IC,INIT}$ and $G_{IC,PROP}$ values for all samples: G-0.5LP sample (0.5 h at 1.8×10^{-2} Torr), G-1LP sample (1 h at 1.8×10^{-2} Torr), and G-0.5HP sample (0.5 h at 3×10^{-2} Torr).

Table 1. G_{IC} and G_{IIC} Values for all Fabricated Composites

sample	$G_{IC,PROP}$ (J m^{-2})	$G_{IC,INIT}$ (J m^{-2})	percentage of enhancement (%) Prop/Init	$G_{IIC,NPC}$ $G_{IIC,PC}$ (J m^{-2})	percentage of enhancement (%) NPC/PC
bCF	293.2 ± 27.4	225.7 ± 15.1		1169 ± 57	
				1183 ± 20	
G-0.5LP	364.1 ± 34.9	249.4 ± 30.6	24.2/10.5	1262 ± 80	8.0
				1212 ± 38	2.4
G-1LP	408.7 ± 35.7	378.8 ± 41.8	39.4/67.8	1296 ± 69	10.9
				1539 ± 68	30.0
G-0.5HP	480.7 ± 44.9	437.4 ± 24.8	63.9/93.8	1674 ± 71	43.3
				1692 ± 60	43.1

of G-0.5LP and G-1LP and shifting of 2D to higher wavenumbers.

3.2. TEM Analysis. The corrugated-like morphology of the G-1LP sample was confirmed from the low-resolution TEM image of Figure S4a, possessing a wavier appearance compared to that of D-0.5HP (Figure S4c). Edges of graphitic layers can be identified in the high-resolution TEM images of G-1LP and G-0.5HP samples shown in Figure 3a,c, respectively, confirming the multilayer nature of the nanoflakes. An interlayer spacing of 0.34 nm corresponding to the (002) graphitic carbon plane was estimated from the intensity line profiles (Figure 3b,d) along the edges depicted by red lines in Figure 3a,c corroborating with the XRD findings (Figure S5). Numerous images were analyzed to determine the thickness (number of layers) of nanoflakes, the frequency of which is illustrated in the generated histograms of Figure S3b,d. From this analysis, the average number of layers was estimated as ∼11 and ∼20 for G-1LP and G-0.5HP, respectively.

3.3. Mode-I and Mode-II Interlaminar Fracture Toughness Measurements. *3.3.1. Mode-I Interlaminar Fracture Toughness Measurements.* At first, the interlaminar fracture toughness was determined in terms of the mode-I (opening mode) strain energy release rate, denoted as G_{IC} (Figure 4). In mode-I, delamination is demonstrated via crack's initiation and propagation, in the interlaminar region of the DCB, caused by a combination of tensile and shear stresses.[53,54] It should be noted that two different G_{IC} values were calculated for this test, one originating from the crack initiation ($G_{IC,INIT}$) and another one from crack propagation ($G_{IC,PROP}$). All of the G_{IC} values are summarized in Table 1. Following the guidelines of ASTM D5528, the delamination resistance curves (*R*) were constructed using the recorded load−displacement data, which are essentially the graph of G_{IC} versus crack length (*a*) (Figure 4a). The *R* curves (Figure 4a) and the analyzed data (Figure 4b) showed that all GNF composites exhibited increased propagation and initiation G_{IC} when compared to the control bCF laminate. This indicates that the GNF interfaces were capable of improving interply adhesion and resistance of the initiation and propagation of cracks in CFRPs. More specifically, the G-1LP specimen showed boosts of 67.8% and 39.4% in $G_{IC,INIT}$ and $G_{IC,PROP}$ values, respectively, whereas G-0.5LP displayed enhancements of 10.5% and 24.2%, respectively, reflecting a rather weaker interlaminar region in comparison to G-1LP, however stronger in comparison to the bare CF composite. The best toughening effect was observed for the highly dense G-0.5HP displaying improvements of 93.8% ($G_{IC,INIT}$) and 63.9% ($G_{IC,PROP}$). The *R* curves show that G_{IC} values were gradually amplified within the crack growth phase between 50 and 70 mm and reached steady-state fracture toughness values at delamination length values above 70 mm, with only exception for the G-0.5HP sample, where saturation of the fracture toughness was attained at 80 mm of the delamination length. This is the outcome of extensive fiber bridging induced by the reinforcing GNF interface, which provided greater resistance in the direction of the propagating crack.

For a comprehensive interpretation of the mode-I results, it is important to elucidate the toughening mechanisms that were responsible for the CFRP's fracture toughness enhancement. For this reason, examination of post-failure SEM micrographs (Figure 5) of fractured surfaces was conducted to deduce

https://doi.org/10.1021/acsanm.1c01722
ACS Appl. Nano Mater. XXXX, XXX, XXX−XXX

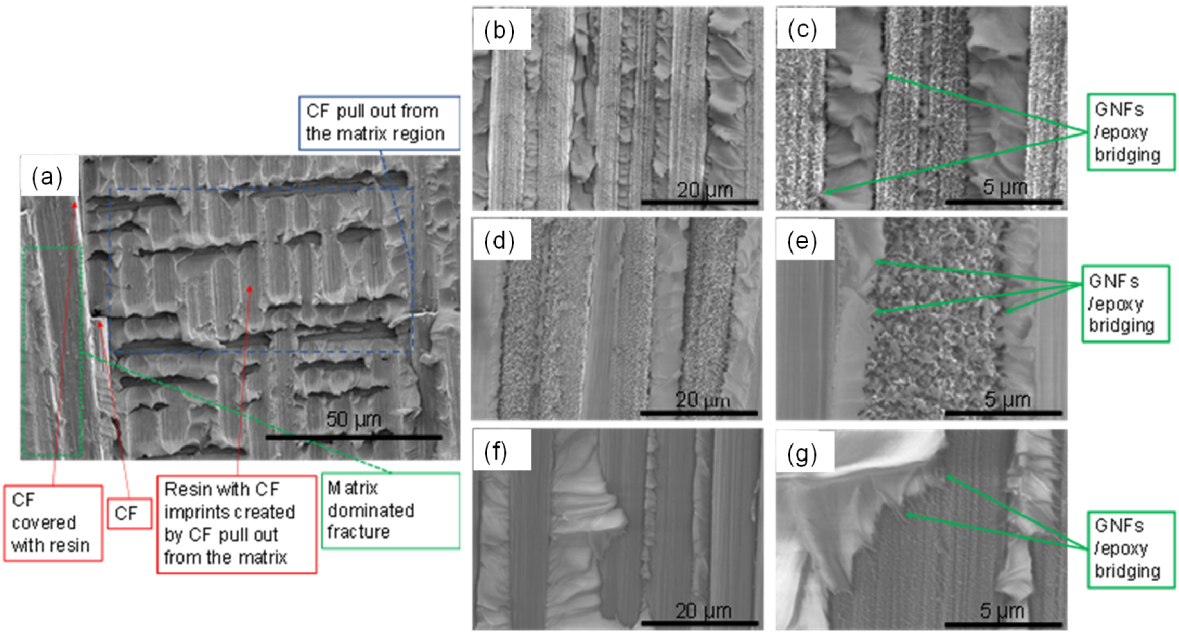

Figure 5. Post-failure SEM micrographs. (a) bCF (reference sample), (b and c) G-0.5LP sample (0.5 h at 1.8×10^{-2} Torr), (d and e) G-1LP sample (1 h at 1.8×10^{-2} Torr), and (f and g) G-0.5HP (0.5 h at 3×10^{-2} Torr).

information about the damage and toughening mechanisms. The fractured surfaces of the GNF-containing composites were distinctly different from those of the control composites, suggesting mechanistic changes in the fracture process. From the fractographic analysis of the bCF sample (Figure 5a), it can be seen that no bridging effects between the epoxy resin and the grown GNFs were detected, indicating a brittle interface. The smooth and nonroughened surface of the reference sample indicates that the fibers were pulled out from the matrix easily, absorbing less amount of fracture energy. On the other hand, all GNF-incorporated samples presented bridging effects between the resin and the GNFs, as can be seen in Figure 5b–f, where remaining resin traces were visible on the surface of the GNF/CF hybrids. As mentioned earlier, all GNF/CF samples exhibited an increase in the fracture toughness (from 24.2% to 93.8%) with respect to control bare CFs (bCFs). The labyrinth-like structure of the graphene flakes increased the surface area of the CFs when compared to the smooth and featureless bCF surface. This extra porosity that GNFs provided allowed for the epoxy resin to infiltrate through this labyrinth-like structure, resulting in a strong matrix–GNF interface. The enhanced interface absorbed more fracture energy than the bare bCF/epoxy interface, and as a result, the G_{IC} values increased. Even though all GNFs provided a toughening effect, it seems that the degree of waviness and density of GNFs played a key role in strengthening the interlaminar region. The G-0.5HP sample included a larger number of sharp vertical and less wavy graphene edges, when compared to the other two composite samples (G-1LP and G-0.5LP), allowing better interlocking with the epoxy matrix. The almost 25% enhancement in propagation fracture toughness of G-1LP compared to G-0.5LP is related to the larger height of G-1LP, which provided larger GNF/epoxy interfaces. It should be noted that X-ray photoelectron spectroscopy (XPS) (Figure S6 and Tables S3 and S4) did not reveal any observable differences in the oxygen atomic concentration among the three samples, suggesting similar interactions between the GNFs and the epoxy.

3.3.2. Mode-II Interlaminar Fracture Toughness Measurements. The interlaminar fracture toughness was also examined in terms of the mode-II strain energy release rate (G_{IIC}) (Figures S9–S11). The results of G_{IIC} (Figure 6 and Table 1) followed

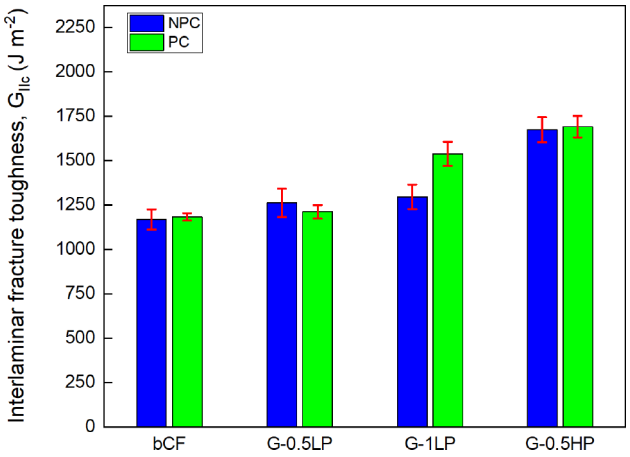

Figure 6. Mode-II (G_{IIC}) values for all samples for both NPC and PC tests: G-0.5LP sample (0.5 h at 1.8×10^{-2} Torr), G-1LP sample (1 h at 1.8×10^{-2} Torr), and G-0.5HP sample (0.5 h at 3×10^{-2} Torr).

the same trendline as the G_{IC} results, with the G-0.5HP sample presenting the best performance of about 43.3% and 43.1% in NPC and PC tests, respectively. The next best sample was the G-1LP with 10.9% and 30.0% again in NPC and PC tests, respectively, whereas the G-0.5LP presented a slight increase in the mode-II fracture toughness of about 8.0% and 2.4%, respectively. It should be noted that all samples presented almost linear behavior up to the maximum point (P_{max}). However, even though the G_{IC} and G_{IIC} results are in agreement regarding the GNF-reinforced interlaminar region of the laminates, it is very clear that the percentages of the enhancement are greater in the case of mode-I tests (maximum values observed: 93.8% vs 43.3%). The divergence in the enhancement between G_{IC} and

https://doi.org/10.1021/acsanm.1c01722
ACS Appl. Nano Mater. XXXX, XXX, XXX−XXX

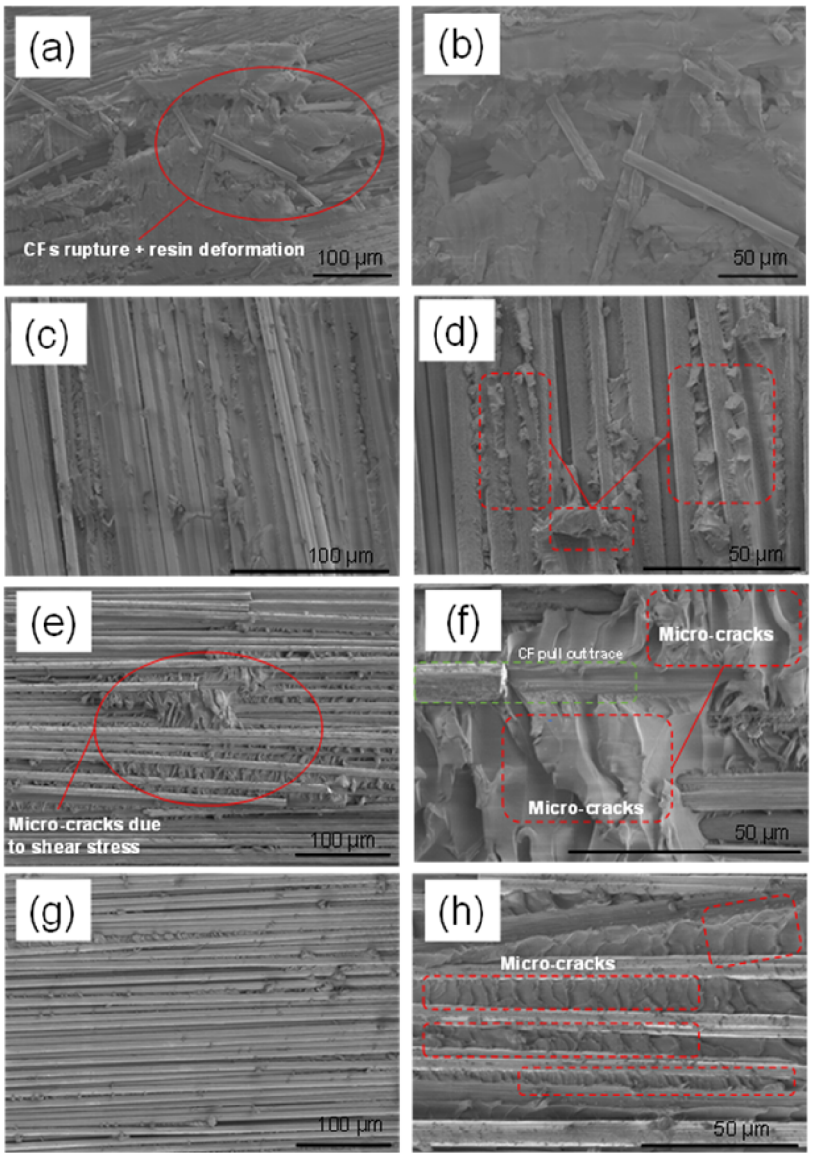

Figure 7. Post-failure fractographic analysis of mode-II tested samples. (a and b) bCF, (c and d) G-0.5LP, (e and f) G-1LP, and (g and h) G-0.5HP sample. G-0.5LP sample (0.5 h at 1.8×10^{-2} Torr), G-1LP sample (1 h at 1.8×10^{-2} Torr), and G-0.5HP sample (0.5 h at 3×10^{-2} Torr).

G_{IIC} relies on the fact that the GNFs are more sensitive to interlaminar crack propagation induced under opening load conditions (mode-I tests). This can be attributed to the different nature of stresses manifested during these two tests, where the crack growth is driven by tensile stress in mode-I tests and by shear stress in mode-II. It seems that the direction of the offside microseparations played a crucial role in these two different failure modes. In mode-I, lateral growth of microseparations is happening, whereas there is no such predilection for mode-II if the compressive stress is adequately strong.[55] For a better understanding of the failure mechanism in mode-II tests, post-failure SEM micrographs were acquired (Figure 7).

The post-failure micrographs (Figure 7) revealed that all GNF-incorporated laminates presented a "rougher" surface when compared to the control bCF laminate. At the fractured surface of the GNF samples, microcracks (hackles) were present, which is a microfractographic characteristic of interlaminar fracture due to shear stresses. Hackles start in the form of microcracks, induced by local tensile stresses on the interlaminar sheared region. As the microcracks grow, they reach the fiber ply and change the direction due to the existence of GNFs.[56,57] This hackle pattern is indicative of a shear stress dominant state,[58] not seen in the mode-I tests. The bCF sample (Figure 7a,b) presented numerous CF ruptures and resin deformation, with no apparent hackle patterns. G-0.5LP exhibited a moderate population of hackles (Figure 7e,f) with large lateral dimensions, which agrees with the observed moderate enhancement in G_{IIC}. On the other hand, the hackles in G-1LP (Figure 7c,d) and G-0.5HP (Figure 7g,h) samples were numerous and denser, and that was the reason they demonstrated the best results in mode-II PC tests. The G-0.5HP sample was the one with the best performance in both NPC and PC tests (43.3% and 43.1%, respectively). From the post-failure analysis, it can be seen that shear stress induced hackles possessing smaller dimension in comparison to the other samples, but the denser pattern among them. The sharper and denser vertical graphene edges of the G-0.5HP sample resisted the matrix cracking, by deflecting the main crack into smaller numerous microcracks (hackles), and therefore amplified the

https://doi.org/10.1021/acsanm.1c01722
ACS Appl. Nano Mater. XXXX, XXX, XXX−XXX

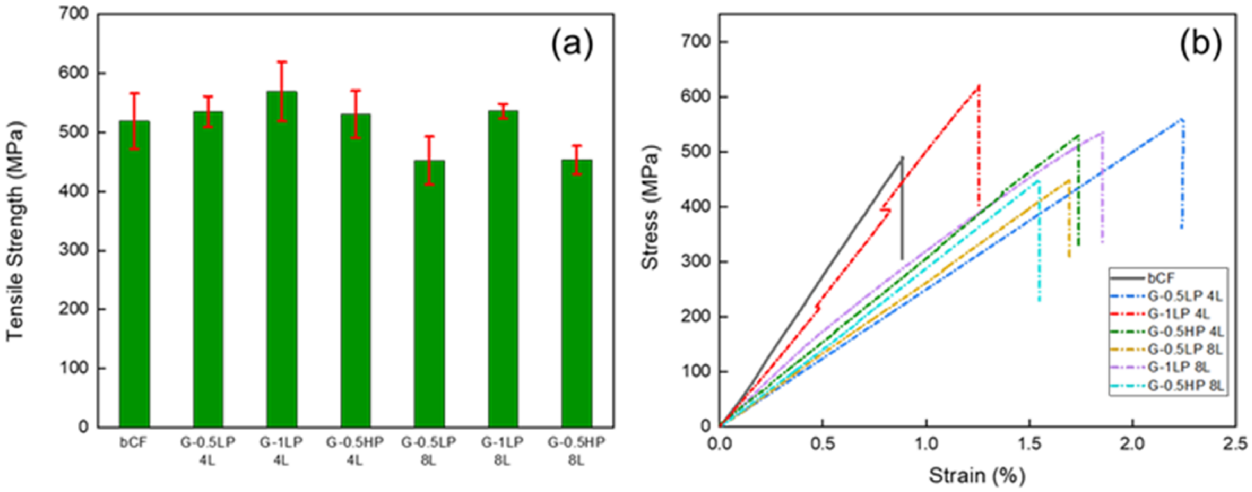

Figure 8. Tensile strength results of all fabricated samples. (a) Tensile strength average values of control and GNFs composites and (b) representative stress−strain curves for all samples. Error bars represent standard deviation from five independent measurements. G-0.5LP sample (0.5 h at 1.8×10^{-2} Torr), G-1LP sample (1 h at 1.8×10^{-2} Torr), and G-0.5HP sample (0.5 h at 3×10^{-2} Torr).

fracture energy absorption required for crack initiation and propagation.

3.4. Tensile Strength Measurements of Fabricated Composites. Tensile strength measurements of the produced composited were carried out to determine the effect of directly grown GNFs on the in-plane properties of woven fabrics. So far, the tensile strength of GNFs/CFs has not been investigated. The only relative work included interlaminar shear strength (ILSS) tests on GNFs/CFs laminates, but no tensile strength tests were reported.[40]

In our tensile strength tests, the stacking sequence and number of the CF/GNF fabrics incorporated in the laminates were investigated. As was described earlier in Section 2.4 (Figure S2), two configurations were studied. In the first one, two CF/GNF fabrics were placed in the midplane of the laminate facing each other, whereas another two were positioned at the outer sides aiming for an increased in-plane electrical conductivity. In the second configuration, the effect of introducing additional CF/GNFs pairs (3) on the tensile strength was examined.

Figure 8a and Table 2 present the average tensile strength values of the fabricated composites incorporating each four and eight layers (L) in total, whereas in Figure 8b, representative stress−strain curves are illustrated. The G-1LP 4L specimen exhibited an enhancement of about 9.7%; in contrast, the tensile strengths of G-0.5LP 4L and G-0.5HP 4L were found to be almost unchanged within the statistical variation with respect to control specimens. The preserved tensile strength indicates that the GNFs do not act as defects or microstress concentration sites in the composite. The reinforcement of G-1LP 4L is attributed to the taller and longer GNFs when compared to G-0.5LP and G-0.5HP-3 4L laminates. This increased aspect ratio (height/lateral length) of the GNFs in G-1LP provided more effective stress transfer load, when compared to the rest of the samples. Moreover, from the TEM analysis (Figure 3), ∼11 graphene layers can be observed for the G-1LP sample, whereas ∼20 layers can be seen for the G-0.5HP sample. The larger number of layers in G-0.5HP may contribute to less efficient stress transfer due to slippage between the internal graphene layers,[59] resulting in less reinforcement in its tensile strength, when compared to the G-1LP sample (11 layers). Another reason that the G-1LP exhibited increased tensile strength is the spatial orientation of the GNFs. Generally, the spatial orientation of the GNFs is very critical for the CFRP enhancement, as the reinforcement is greater when the flakes are aligned in the direction of strain.[31,60] In the G-1LP sample, many of the formed corrugated flakes are oriented almost parallel to the strain direction, whereas the majority of flakes in the G-0.5HP sample are vertical to the strain direction.

Table 2. Tensile Strength Values of the Composite Materials

sample	tensile strength (MPa)	error (MPa)
bCF	519	47
G-0.5LP 4L	535	26
G-1LP 4L	569	25
G-0.5HP 4L	531	40
G-0.5LP 8L	452	41
G-1LP 8L	536	12
G-0.5HP 8L	454	24

Increasing the number of CF/GNF (8L) in the laminate structure led to an overall decrease in tensile strength compared to the reduced layer (4L) configuration. However, still G-1LP 8L preserved the tensile strength of the control, whereas G-0.5LP 8L and G-0.5HP 8L exhibited decrements of about 12.8% and 12.6%, respectively.

It is worth emphasizing that in the reported literature (Table S5), the simultaneous investigation of fracture toughness (in terms of modes I and II) and tensile strength of nanoenhanced CFRP composites is very rare or nonexistent. Importantly, this is the first work that reports these mechanical tests on GNF nanoreinforced laminated composites; to date, the only work on laminated GNF composites has investigated ILSS.[40]

3.5. Electrical Conductivity Measurements and Multifunctionality of Fabricated Composites. Electrical conductivity (S cm^{-1}) of all fabricated composites was measured on both in-plane (*xy* direction) and out-of-plane through-volumes (*z* direction) to evaluate the role of directly grown GNFs in the electrical behavior of composites (Figure 9). The conductivity values are quoted in Table 3. From the results, it can be seen that the best behavior on the electrical conductivity was exhibited by the G-1LP 8L (8 deposited layers) sample, reporting enhancement in both the in-plane and out-of-plane conductivity up to 45% and 527%, respectively (CGF-1 8L). The next best sample

https://doi.org/10.1021/acsanm.1c01722
ACS Appl. Nano Mater. XXXX, XXX, XXX−XXX

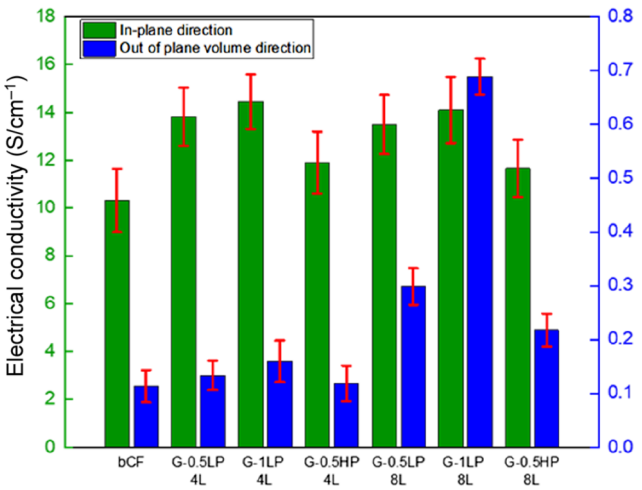

Figure 9. Electrical conductivity of all fabricated composites for both in-plane and out-of-plane through-volume directions. G-0.5LP sample (0.5 h at 1.8×10^{-2} Torr), G-1LP sample (1 h at 1.8×10^{-2} Torr), and G-0.5HP sample (0.5 h at 3×10^{-2} Torr).

Table 3. Electrical Conductivity of all Fabricated Samples

sample	in-plane (xy) direction (S cm^{-1})	out-of-plane through-volume direction (z) (S cm^{-1})
bCF	10.32 ± 1.33	0.11 ± 0.03
G-0.5LP 4L	13.82 ± 1.21	0.13 ± 0.03
G-1LP 4L	14.45 ± 1.13	0.16 ± 0.04
G-0.5HP 4L	11.91 ± 1.29	0.12 ± 0.03
G-0.5LP 8L	13.50 ± 1.23	0.30 ± 0.03
G-1LP 8L	14.10 ± 1.37	0.69 ± 0.03
G-0.5HP 8L	11.67 ± 1.19	0.22 ± 0.03

was G-0.5LP 8L with estimated values of reinforcement up to 37% and 163%, whereas the G-0.5HP 8L sample showed an increment up to 16% and 91%. It is clear that the sample with the largest aspect ratio of the graphene flakes (G-1LP) showed the best results in the electrical conductivity, with the G-1LP 8L sample demonstrating a tremendous enhancement of 527% on out-of-plane volume values. This improved transport is mainly attributed to the longer GNFs that provided larger conductive paths of the current flow between the CF layers in the laminate. It should be noted here that all of the 8L samples (CGF-1 8L, G-0.5LP 8L, and G-0.5HP 8L) exhibited a remarkable increment in their out-of-plane through-volume conductivity when compared to the 4L ones (G-1LP 4L, G-0.5LP 4L, and G-0.5HP 4L), which is consistent with the dominant role of the larger number of the conductive CF/GNF hybrid layers (8 out of 12) incorporated in the laminated structure.

3.5.1. Multifunctional Assessment of the Composites. The electrical properties of CFs used as a nanoreinforcement in laminated structures are the starting point for various multifunctional applications, including structural health monitoring, de-icing, lighting strike protection, electromagnetic shielding, and energy storage.[61] However, one important challenge in imparting these multifunctional attributes in CFRPs is their poor out-of-plane conductivity, which originates from the low strength, ductile, electrically, and thermally insulating polymer matrix. A refined approach used here via the incorporation of GNFs attains enhancement on out-of-plane electrical properties of CFRPs simultaneously with improvements in their mechanical properties.

The tensile strength values normalized to control bCF sample (T/T_{bcf}) are plotted against the out-of-plane conductivity normalized to the bCF (S/S_{bcf}) of each sample in order to evaluate the "multifunctional efficiency" of the composite materials (Figure 10). The shaded area in Figure 10 indicates

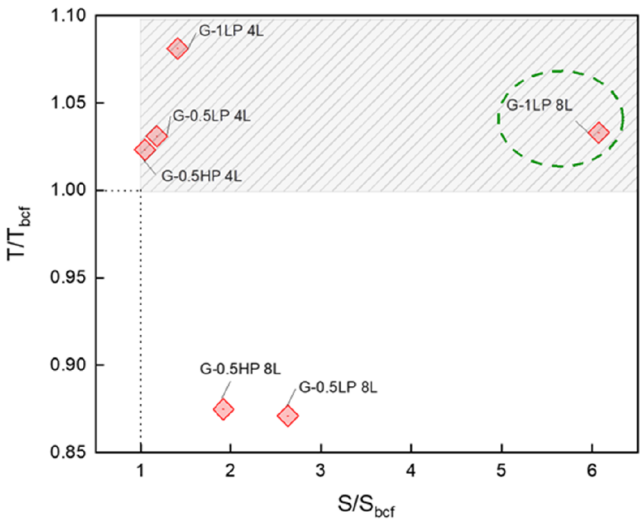

Figure 10. Normalized tensile strength (T/T_{bcf}) vs normalized electrical conductivity (S/S_{bcf}) of the fabricated samples. G-0.5LP sample (0.5 h at 1.8×10^{-2} Torr), G-1LP sample (1 h at 1.8×10^{-2} Torr), and G-0.5HP sample (0.5 h at 3×10^{-2} Torr).

improved performance in both tensile strength and electrical conductivity compared to bCF. It is clear that the G-1LP 8L sample is the most promising one where its tensile strength was preserved (slightly increased), while its conductivity exhibited a remarkable reinforcement of about 527%. On the other hand, the G-1LP 4L sample showed an increase of about 9.7% in its tensile strength, whereas the out-of-plane conductivity improved by 45%, making itself a strong candidate in applications where stronger materials are needed and the enhancement of the electrical conductivity is not the primary target.

4. CONCLUSIONS

This work has demonstrated for the first time the direct growth of oriented GNFs onto the surface of CF fabrics as an effective approach to significantly toughen the interlaminar region of CFRP matrix composites and at the same time to enhance the tensile strength and out-of-plane conductivity. The mechanical characteristics of the composites were controlled by modifying the surface morphology of the nanoflakes (density and waviness) through adjusting the deposition conditions. This is the first work in the literature reporting both mode-I and mode-II interlaminar fracture toughness and tensile strength tests on CFRP with a GNF interface. The direct growth of the GNFs on CF fabrics led to a significant reinforcement of mode-I and mode-II interlaminar fracture toughness up to 93.8% and 43.3%, respectively. The GNF interfaces at the interlaminar region provided higher resistance to crack initiation and propagation through a combination of mechanisms, such as (i) enhanced fiber−matrix bridging due to the GNFs' waviness, (ii) efficient interlocking of the graphene flakes' 3D network with the resin matrix, and (iii) crack deflection into denser numerous microcracks (hackles). All of the above toughening mechanisms were attributed mainly to the morphology of the GNFs grown onto the CFs, where the degree of waviness and density of them

https://doi.org/10.1021/acsanm.1c01722
ACS Appl. Nano Mater. XXXX, XXX, XXX−XXX

played a key role in strengthening the interlaminar region of the produced composites.

Our results demonstrated that by tailoring the graphene flakes' aspect ratio and waviness, it is possible to achieve larger values of tensile strength reinforcement. The corrugated and wrinkled nature of G-1LP introduced by the low pressure deposition conditions, along with the reduced number of graphene layers that reduced slippage phenomena between the graphene layers, ensured efficient stress transfer and hence moderately increased/maintained the tensile strength of the fabricated CFRP, introducing a new way to reinforce the interlaminar properties of the CFRP without degrading their tensile strength. Additionally, the number and sequence of GNF/CF fabrics had a significant effect on the tensile strength. In a 4 GNF layer configuration, where two GNF fabrics were placed in the midplane and another two at the outer side of the laminate, the tensile strength of the composite was improved by 9.7%. However, the incorporation of eight deposited layers into the composite structure led to a decreased tensile strength for G-0.5LP and G-0.5HP samples and a preserved strength for the G-1LP sample, indicating that incorporation of a larger amount of hybrid fabrics in the laminate could negatively affect the tensile strength of the composites. The enhancement of tensile strength at four layers is an advantage as the incorporation of more deposited layers into the laminated structure could possibly be more time consuming and costly.

The electrical properties of the produced composites were assessed through conductivity measurements on both in-plane and out-of-plane through-volume directions. The results revealed that G-1LP samples showed larger values of reinforcement in conductivity when compared with G-0.5LP and G-0.5HP composites, indicating that larger flakes could possibly create larger conductive paths for the flow current and as a result higher values of electrical conductivity. When eight layers of deposited fabrics were incorporated into the laminated structure, the out-of-plane through-volume conductivity was remarkably enhanced, reporting values of reinforcement up to 527%, demonstrating that the incorporation of more coated layers could lead to larger enhancement of the out-of-plane conductivity. Generally, the results of this work demonstrated for the first time the huge potential of a GNF interface for multifunctional laminates, as both mechanical and electrical performance of the fabricated composites were increased under certain GNF growth conditions, indicating that the rf-PECVD method is suitable for all around properties' reinforcement. The work provided new insights into reinforcement mechanisms at work and acts as a guide for the design of future nanoreinforced CFRPs.

■ ASSOCIATED CONTENT

Supporting Information

The Supporting Information is available free of charge at https://pubs.acs.org/doi/10.1021/acsanm.1c01722.

> GNFs growth conditions and 3D optical illustration of all grown GNF morphologies; VARI procedure; Raman analysis of all grown GNF samples; TEM analysis of G-1LP and G-0.5HP samples; XRD analysis of G-1LP and G-0.5HP samples; XPS analysis; mode-I interlaminar fracture toughness measurements; mode-II interlaminar fracture toughness measurements; tensile strength tests; electrical conductivity measurements; and comparative table of reported studies on CFRP (PDF)

■ AUTHOR INFORMATION

Corresponding Author

Pagona Papakonstantinou − *School of Engineering, Engineering Research Institute, Ulster University, Belfast BT15 1ED, U.K.;* orcid.org/0000-0003-0019-3247; Email: p.papakonstantinou@ulster.ac.uk

Authors

Anastasios Karakassides − *School of Engineering, Engineering Research Institute, Ulster University, Belfast BT15 1ED, U.K.;* orcid.org/0000-0002-1324-5301

Abhijit Ganguly − *School of Engineering, Engineering Research Institute, Ulster University, Belfast BT15 1ED, U.K.;* orcid.org/0000-0002-8852-2721

John Kelly − *School of Engineering, Engineering Research Institute, Ulster University, Belfast BT15 1ED, U.K.*

Preetam K. Sharma − *School of Engineering, Engineering Research Institute, Ulster University, Belfast BT15 1ED, U.K.;* orcid.org/0000-0002-5694-8445

Complete contact information is available at: https://pubs.acs.org/10.1021/acsanm.1c01722

Author Contributions

The manuscript was written through contributions of all authors. All authors have given approval to the final version of the manuscript.

Notes

The authors declare no competing financial interest.

■ ACKNOWLEDGMENTS

The authors acknowledge the support from the Air Force Office of Scientific Research (AFOSR) under grant no. FA9550-17-1-0042 and the Department for the Economy (DfE) in Northern Ireland and Ulster University for providing a Ph.D. studentship to A.K.

■ REFERENCES

(1) Das, R.; Melchior, C.; Karumbaiah, K. M. Self-Healing Composites for Aerospace Applications. In *Advanced Composite Materials for Aerospace Engineering*, Chapter 11; Elsevier, 2016; 333−364.

(2) Dold, C.; Henerichs, M.; Bochmann, L.; Wegener, K. Comparison of Ground and Laser Machined Polycrystalline Diamond (PCD) Tools in Cutting Carbon Fiber Reinforced Plastics (CFRP) for Aircraft Structures. *Proc. CIRP* **2012**, *1*, 178−183.

(3) Friedrich, K.; Almajid, A. A. Manufacturing Aspects of Advanced Polymer Composites for Automotive Applications. *Appl. Compos. Mater.* **2013**, *20*, 107−128.

(4) Olofin, I.; Liu, R. The Application of Carbon Fibre Reinforced Polymer (CFRP) Cables in Civil Engineering Structures. *Int. J. Civ. Eng.* **2015**, *2*, 1−5.

(5) ASTM International. *Standard Test Method for Mode I Interlaminar Fracture Toughness of Unidirectional Fiber-Reinforced Polymer Matrix Composites*; ASTM D5528-01, 2014

(6) ASTM International. *Standard Test Method for Determination of the Mode II Interlaminar Fracture Toughness of Unidirectional Fiber-Reinforced Polymer Matrix Composites*; ASTM D7905, 2014.

(7) Ritchie, R. O. The Conflicts between Strength and Toughness. *Nat. Mater.* **2011**, *10*, 817−822.

(8) Huang, W.; Restrepo, D.; Jung, J.; Su, F. Y.; Liu, Z.; Ritchie, R. O.; McKittrick, J.; Zavattieri, P.; Kisailus, D. Multiscale Toughening Mechanisms in Biological Materials and Bioinspired Designs. *Adv. Mater.* **2019**, *31*, No. 1901561.

(9) Mouritz, A. P.; Bannister, M. K.; Falzon, P. J.; Leong, K. H. Review of Applications for Advanced Three-Dimensional Fibre Textile Composites. *Composites, Part A* **1999**, *30*, 1445−1461.
(10) Dransfield, K.; Baillie, C.; Mai, Y. W. Improving the Delamination Resistance of CFRP by Stitching-a Review. *Compos. Sci. Technol.* **1994**, *50*, 305−317.
(11) Tong, L.; Mouritz, A. P.; Bannister, M. K. Stitched Composites. In *3D Fibre Reinforced Polymer Composites*, Vol. *13*; Elsevier, 2002; 163−204.
(12) Mouritz, A. P. Review of Z-Pinned Composite Laminates. *Composites, Part A* **2007**, *38*, 2383−2397.
(13) Ansar, M.; Xinwei, W.; Chouwei, Z. Modeling Strategies of 3D Woven Composites: A Review. *Compos. Struct.* **2011**, *93*, 1947−1963.
(14) Behera, B. K.; Mishra, R. 3-Dimensional Weaving. *Indian J. Fibre Text. Res.* **2008**, *33*, 274−287.
(15) Khokar, N. 3D-Weaving: Theory and Practice. *J. Text. Inst.* **2001**, *92*, 193−207.
(16) Bilisik, K. Three-Dimensional Braiding for Composites: A Review. *Text. Res. J.* **2013**, *83*, 1414−1436.
(17) Steeves, C. A.; Fleck, N. A. In-Plane Properties of Composite Laminates with through-Thickness Pin Reinforcement. *Int. J. Solids Struct.* **2006**, *43*, 3197−3212.
(18) Quan, D.; Bologna, F.; Scarselli, G.; Ivankovic, A.; Murphy, N. Interlaminar Fracture Toughness of Aerospace-Grade Carbon Fibre Reinforced Plastics Interleaved with Thermoplastic Veils. *Composites, Part A* **2020**, *128*, No. 105642.
(19) García-Rodríguez, S. M.; Costa, J.; Rankin, K. E.; Boardman, R. P.; Singery, V.; Mayugo, J. A. Interleaving Light Veils to Minimise the Trade-off between Mode-I Interlaminar Fracture Toughness and in-Plane Properties. *Composites, Part A* **2020**, *128*, No. 105659.
(20) İnal, O.; Akbolat, M. Ç.; Soutis, C.; Katnam, K. B. Toughening Mechanisms in Cost-Effective Carbon-Epoxy Laminates with Thermoplastic Veils: Mode-I and in-Situ SEM Fracture Characterisation. *Int. J. Lightweight Mater. Manuf.* **2021**, *4*, 50−61.
(21) Kaynan, O.; Atescan, Y.; Ozden-Yenigun, E.; Cebeci, H. Mixed Mode Delamination in Carbon Nanotube/Nanofiber Interlayered Composites. *Composites, Part B* **2018**, *154*, 186−194.
(22) Beckermann, G. W.; Pickering, K. L. Mode I and Mode II Interlaminar Fracture Toughness of Composite Laminates Interleaved with Electrospun Nanofibre Veils. *Composites Part A* **2015**, *72*, 11−21.
(23) Quan, D.; Mischo, C.; Li, X.; Scarselli, G.; Ivanković, A.; Murphy, N. Improving the Electrical Conductivity and Fracture Toughness of Carbon Fibre/Epoxy Composites by Interleaving MWCNT-Doped Thermoplastic Veils. *Compos. Sci. Technol.* **2019**, *182*, No. 107775.
(24) Quan, D.; Deegan, B.; Alderliesten, R.; Dransfeld, C.; Murphy, N.; Ivanković, A.; Benedictus, R. The Influence of Interlayer/Epoxy Adhesion on the Mode-I and Mode-II Fracture Response of Carbon Fibre/Epoxy Composites Interleaved with Thermoplastic Veils. *Mater. Des.* **2020**, *192*, No. 108781.
(25) Ramji, A.; Xu, Y.; Grasso, M.; Yasaee, M.; Webb, P. Effect of Interfacial Fibre Orientation and PPS Veil Density on Delamination Resistance of 5HS Woven CFRP Laminates under Mode II Loading. *Compos. Sci. Technol.* **2021**, *207*, No. 108735.
(26) Wang, W.; Yue, X.; Zhang, C.; Wu, J.; Wang, C.; Huang, H.; Zhu, P. *Mechanical and Piezo-Resistance Behavior of CNTs/Epoxy Resin Composite for Structural Health Monitoring. 26th International Conference on Optical Fiber Sensors*; OSA: Washington, D.C., 2018; ThE92.
(27) Ma, P. C.; Mo, S. Y.; Tang, B. Z.; Kim, J. K. Dispersion, Interfacial Interaction and Re-Agglomeration of Functionalized Carbon Nanotubes in Epoxy Composites. *Carbon* **2010**, *48*, 1824−1834.
(28) Wladyka-Przybylak, M.; Wesolek, D.; Gieparda, W.; Boczkowska, A.; Ciecierska, E. The Effect of the Surface Modification of Carbon Nanotubes on Their Dispersion in the Epoxy Matrix. *Pol. J. Chem. Technol.* **2011**, *13*, 62−69.
(29) Shen, M. Y.; Chang, T. Y.; Hsieh, T. H.; Li, Y. L.; Chiang, C. L.; Yang, H.; Yip, M. C. Mechanical Properties and Tensile Fatigue of Graphene Nanoplatelets Reinforced Polymer Nanocomposites. *J. Nanomater.* **2013**, *2013*, No. 565401.
(30) Wang, P. N.; Hsieh, T. H.; Chiang, C. L.; Shen, M. Y. Synergetic Effects of Mechanical Properties on Graphene Nanoplatelet and Multiwalled Carbon Nanotube Hybrids Reinforced Epoxy/Carbon Fiber Composites. *J. Nanomater.* **2015**, *2015*, No. 838032.
(31) Papageorgiou, D. G.; Li, Z.; Liu, M.; Kinloch, I. A.; Young, R. J. Mechanisms of Mechanical Reinforcement by Graphene and Carbon Nanotubes in Polymer Nanocomposites. *Nanoscale* **2020**, *20*, 2228.
(32) Shtein, M.; Nadiv, R.; Lachman, N.; Daniel Wagner, H.; Regev, O. Fracture Behavior of Nanotube−Polymer Composites: Insights on Surface Roughness and Failure Mechanism. *Compos. Sci. Technol.* **2013**, *87*, 157−163.
(33) Ivanov, E.; Velichkova, H.; Kotsilkova, R.; Bistarelli, S.; Cataldo, A.; Micciulla, F.; Bellucci, S. Rheological Behavior of Graphene/Epoxy Nanodispersions. *Appl. Rheol.* **2017**, *27*, 1−9.
(34) Zhang, H.; Liu, Y.; Kuwata, M.; Bilotti, E.; Peijs, T. Improved Fracture Toughness and Integrated Damage Sensing Capability by Spray Coated CNTs on Carbon Fibre Prepreg. *Composites, Part A* **2015**, *70*, 102−110.
(35) Ou, Y.; González, C.; Vilatela, J. J. Understanding Interlaminar Toughening of Unidirectional CFRP Laminates with Carbon Nanotube Veils. *Composites, Part B* **2020**, *201*, No. 108372.
(36) Garcia, E. J.; Wardle, B. L.; John Hart, A. Joining Prepreg Composite Interfaces with Aligned Carbon Nanotubes. *Composites, Part A* **2008**, *39*, 1065−1070.
(37) Chi, Y.; Chu, J.; Chen, M.; Li, C.; Mao, W.; Piao, M.; Zhang, H.; Liu, B. S.; Shi, H. Directly Deposited Graphene Nanowalls on Carbon Fiber for Improving the Interface Strength in Composites. *Appl. Phys. Lett.* **2016**, *108*, No. 211601.
(38) Sha, Z.; Han, Z.; Wu, S.; Zhang, F.; Islam, M. S.; Brown, S. A.; Wang, C. H. Low-Temperature Plasma Assisted Growth of Vertical Graphene for Enhancing Carbon Fibre/Epoxy Interfacial Strength. *Compos. Sci. Technol.* **2019**, *184*, No. 107867.
(39) Karakassides, A.; Ganguly, A.; Tsirka, K.; Paipetis, A. S.; Papakonstantinou, P. Radially Grown Graphene Nanoflakes on Carbon Fibers as Reinforcing Interface for Polymer Composites. *ACS Appl. Nano Mater.* **2020**, *3*, 2402−2413.
(40) Wang, X.; Li, C.; Chi, Y.; Piao, M.; Chu, J.; Zhang, H.; Li, Z.; Wei, W. Effect of Graphene Nanowall Size on the Interfacial Strength of Carbon Fiber Reinforced Composites. *Nanomaterials* **2018**, *8*, 414.
(41) Zhao, J.; Shaygan, M.; Eckert, J.; Meyyappan, M.; Rümmeli, M. H.; Growth, A. Mechanism for Free-Standing Vertical Graphene. *Nano Lett.* **2014**, *14*, 3064−3071.
(42) Zhang, Z. Y.; Lee, C. S.; Zhang, W. J. Vertically Aligned Graphene Nanosheet Arrays: Synthesis, Properties and Applications in Electrochemical Energy Conversion and Storage. *Adv. Energy Mater.* **2017**, *7*, No. 1700678.
(43) ASTM International. *Standard Test Method for Tensile Properties of Polymer Matrix Composite Materials*, ASTM D3039/D3039M-14, 2014.
(44) Zhu, M.; Wang, J.; Holloway, B. C.; Outlaw, R. A.; Zhao, X.; Hou, K.; Shutthanandan, V.; Manos, D. M. A Mechanism for Carbon Nanosheet Formation. *Carbon* **2007**, *45*, 2229−2234.
(45) Zhang, T.; Li, X.; Gao, H. Defects Controlled Wrinkling and Topological Design in Graphene. *J. Mech. Phys. Solids* **2014**, *67*, 2−13.
(46) Ferrari, A. C.; Basko, D. M. Raman Spectroscopy as a Versatile Tool for Studying the Properties of Graphene. *Nat. Nanotechnol.* **2013**, *8*, 235−246.
(47) Cançado, L. G.; Jorio, A.; Ferreira, E. H. M.; Stavale, F.; Achete, C. A.; Capaz, R. B.; Moutinho, M. V. O.; Lombardo, A.; Kulmala, T. S.; Ferrari, A. C. Quantifying Defects in Graphene via Raman Spectroscopy at Different Excitation Energies. *Nano Lett.* **2011**, *11*, 3190−3196.
(48) Hao, Q.; Morton, S. M.; Wang, B.; Zhao, Y.; Jensen, L.; Jun Huang, T. Tuning Surface-Enhanced Raman Scattering from Graphene Substrates Using the Electric Field Effect and Chemical Doping. *Appl. Phys. Lett.* **2013**, *102*, No. 011102.
(49) Ferrari, A. C.; Meyer, J. C.; Scardaci, V.; Casiraghi, C.; Lazzeri, M.; Mauri, F.; Piscanec, S.; Jiang, D.; Novoselov, K. S.; Roth, S.; Geim, A. K. Raman Spectrum of Graphene and Graphene Layers. *Phys. Rev. Lett.* **2006**, *97*, No. 187401.

https://doi.org/10.1021/acsanm.1c01722
ACS Appl. Nano Mater. XXXX, XXX, XXX−XXX

(50) Yu, Q.; Jauregui, L. A.; Wu, W.; Colby, R.; Tian, J.; Su, Z.; Cao, H.; Liu, Z.; Pandey, D.; Wei, D.; Chung, T. F.; Peng, P.; Guisinger, N. P.; Stach, E. A.; Bao, J.; Pei, S. S.; Chen, Y. P. Control and Characterization of Individual Grains and Grain Boundaries in Graphene Grown by Chemical Vapour Deposition. *Nat. Mater.* **2011**, *10*, 443−449.

(51) Chan, S. H.; Chen, J. W.; Chen, H. P.; Sen, W. H.; Li, M. C.; Chen, S. H.; Lee, C. C.; Kuo, C. C. The Deviation of Growth Model for Transparent Conductive Graphene. *Nanoscale Res. Lett.* **2014**, *9*, No. 581.

(52) Li, Z.; Kinloch, I. A.; Young, R. J.; Novoselov, K. S.; Anagnostopoulos, G.; Parthenios, J.; Galiotis, C.; Papagelis, K.; Lu, C. Y.; Britnell, L. Deformation of Wrinkled Graphene. *ACS Nano* **2015**, *9*, 3917−3925.

(53) Borowski, E.; Soliman, E.; Kandil, U. F.; Taha, M. R. Interlaminar Fracture Toughness of CFRP Laminates Incorporating Multi-Walled Carbon Nanotubes. *Polymers* **2015**, *7*, 1020−1045.

(54) Nasuha, N.; Azmi, A. I.; Tan, C. L. A Review on Mode-I Interlaminar Fracture Toughness of Fibre Reinforced Composites. *J. Phys.: Conf. Ser.* **2017**, *908*, No. 012024.

(55) Broberg, K. B. Differences between Mode I and Mode II Crack Propagation. *Pure Appl. Geophys.* **2006**, *163*, 1867−1879.

(56) Selzer, R.; Krey, J. Fractography of Interlaminar Fracture Surfaces of CF/PI and CF/BMI Composites. *J. Mater. Sci.* **1994**, *29*, 2951−2956.

(57) Shin, Y. C.; Il, L. W.; Kim, H. S. Mode II Interlaminar Fracture Toughness of Carbon Nanotubes/Epoxy Film-Interleaved Carbon Fiber Composites. *Compos. Struct.* **2020**, *236*, No. 111808.

(58) Shivakumar, K. N.; Panduranga, R.; Skujins, J.; Miller, S. Assessment of Mode-II Fracture Tests for Unidirectional Fiber Reinforced Composite Laminates. *J. Reinf. Plast. Compos.* **2015**, *34*, 1905−1925.

(59) Gong, L.; Young, R. J.; Kinloch, I. A.; Riaz, I.; Jalil, R.; Novoselov, K. S. Optimizing the Reinforcement of Polymer-Based Nanocomposites by Graphene. *ACS Nano* **2012**, *6*, 2086−2095.

(60) Lubin, G.; Eds. *Handbook of Composites*; Springer: Boston, US, 1982.

(61) Forintos, N.; Czigany, T. Multifunctional Application of Carbon Fiber Reinforced Polymer Composites: Electrical Properties of the Reinforcing Carbon Fibers − A Short Review. *Composites, Part B* **2019**, *162*, 331−343.

https://doi.org/10.1021/acsanm.1c01722
ACS Appl. Nano Mater. XXXX, XXX, XXX−XXX